Thermophysical properties of 1D materials: transient characterization down to atomic level

Amin Karamati[1,*], Shen Xu[2,*], Huan Lin[3,*], Mahya Rahbar[1,*], and Xinwei Wang[1] ✉

[1]*Department of Mechanical Engineering, Iowa State University, Ames 50011, USA;*

[2]*School of Mechanical and Automotive Engineering, Shanghai University of Engineering Science, Shanghai 201620, China;*
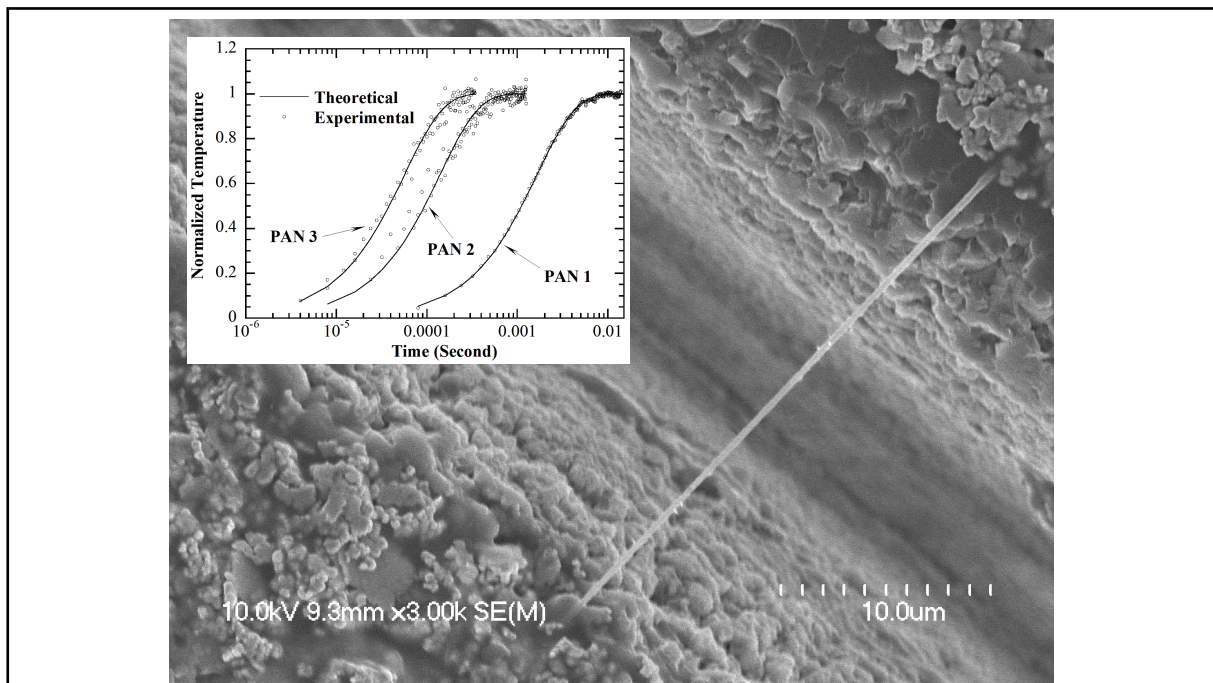
[3]*School of Environmental and Municipal Engineering, Qingdao University of Technology, Qingdao 266033, China*

* These authors contributed equally to this work

✉Correspondence: Xinwei Wang, E-mail: xwang3@iastate.edu

Graphical abstract

SEM image of a nm-thick PAN fiber suspended between two electrodes for TET measurement. The inset shows the data fitting.

Public summary

■ Transient electrothermal (TET) and differential TET techniques provide some of the most advanced characterizations of the thermophysical properties of 1D materials from sub-mm down to atomic thickness.

■ Transient photoelectro-thermal (TPET) and pulsed laser-assisted thermal relaxation (PLTR) techniques offer unique capabilities in measuring 1D materials of extremely high/low resistance or extremely fast thermal characteristic time while they can also measure normal 1D materials.

■ Energy transport state-resolved Raman (ET-Raman) and frequency domain ET-Raman (FET-Raman) provide probably the most advanced measurement of the thermophysical properties of 1D and 2D materials of nm-dimensions with the highest accuracy.

Thermophysical properties of 1D materials: transient characterization down to atomic level

Amin Karamati[1,*], Shen Xu[2,*], Huan Lin[3,*], Mahya Rahbar[1,*], and Xinwei Wang[1] ✉

[1]Department of Mechanical Engineering, Iowa State University, Ames 50011, USA;
[2]School of Mechanical and Automotive Engineering, Shanghai University of Engineering Science, Shanghai 201620, China;
[3]School of Environmental and Municipal Engineering, Qingdao University of Technology, Qingdao 266033, China

* These authors contributed equally to this work
✉Correspondence: Xinwei Wang, E-mail: xwang3@iastate.edu

Abstract: The thermophysical properties of 1D micro/nanoscale materials could differ significantly from those of their bulk counterparts due to intensive energy carrier scattering by structures. This work provides an in-depth review of cutting-edge techniques employed for transient characterization of thermophysical properties at the micro/nanoscale scale. In terms of transient excitation, step Joule heating, step laser heating, pulsed laser heating, and frequency domain amplitude-modulated laser heating are covered. For thermal probing, electrical and Raman scattering-based physical principles are used. These techniques enable the measurement of thermal conductivity, thermal diffusivity, and specific heat from the sub-mm level down to the atomic level (single-atom thickness). This review emphasizes the advantages of these techniques over steady state techniques and their physics, challenges, and potential applications, highlighting their significance in unraveling the intricate thermal transport phenomena to the atomic level of 1D materials.

Keywords: 1D materials; thermophysical properties; transient characterization; Raman scattering; micro/nanoscale

CLC number: TK31; O551.3   **Document code:** A

1   Introduction

The past decades have witnessed significant growing interest in one-dimensional (1D) micro/nanomaterials, which possess unique structural and physical properties. These materials have high aspect ratios, with two dimensions significantly smaller than the third one. Examples of 1D micro/nanomaterials include carbon micro/nanofibers[1], carbon nanotubes (CNTs)[2, 3], silver nanowires[4, 5], and other metallic/semiconductive nanowires[6, 7]. With their specific function design, 1D micro/nanomaterials have become highly attractive for a broad range of applications, including electronics[8, 9], photonics[10, 11], energy storage[12, 13], and sensing[14]. Specifically, in electronics, 1D materials offer the potential to revolutionize the development of high-performance transistors, light-emitting diodes, and solar cells[15, 16]. In photonics, 1D materials have been leveraged to create nanolasers, optical fibers, and photonic crystals[17, 18]. In energy storage, 1D materials are being used to develop high-capacity batteries[19] and supercapacitors[20]. Last not least, 1D materials are also suitable for sensing applications, such as detecting gases[21, 22], chemicals[23], and biomolecules[24]. It is noteworthy that for these applications, the thermophysical properties of 1D micro/nanostructures, particularly thermal conductivity and thermal diffusivity, are critical to thermal design, lifetime, and stability in hostile thermal environments. However, given the novel nature of 1D micro/nanoscale materials, their thermal conductivity/diffusivity differs significantly from those of their bulk counterparts.

The unique physical properties of novel 1D micro/nanoscale materials stem from their thickness/radial dimension, which can be at or below certain characteristic lengths, such as the phonon mean free path, photon absorption depth, or electron mean free path, leading to a very strong size confinement effect[25]. The intensive energy carrier scattering caused by nanostructures and small size in their reduced dimensions significantly reduces the energy carrier's mean free path and thermal conductivity/diffusivity. It is crucial to understand the intrinsic thermal properties of these materials via appropriate thermophysical property measurements. However, the extremely small size of these materials presents great challenges in applying well-defined thermal excitation and characterizing the temperature differential across them[26, 27].

Various methods have been developed to measure the thermophysical properties of 1D micro/nanomaterials, which can be broadly categorized into two types: steady state techniques (such as microbridge and conventional Raman thermometry) and transient techniques (including the 3ω technique, transient hot wire, and flash techniques). Steady state techniques are generally based on simple physical models but require a very careful assessment of boundary conditions and the establishment of a stable and measurable temperature gradient and heat flux. One commonly used steady state technique is the microbridge method[28, 29], which involves the fabrication of a microdevice with two suspended membranes, between which a 1D sample is placed to form a bridge

structure. One membrane serves as a heating element, while the other acts as a temperature sensor. A DC current is passed through the heating membrane to provide stable heat, which then flows through the sample/bridge to the sensing membrane, causing a small temperature rise in the latter. By measuring the temperature of the two membranes, the heat flow through the sample, and the sample's dimensions, the thermal conductivity can be directly determined according to Fourier's law. This technique offers high accuracy and precision and can do the measurement over a wide temperature range, but it also has limitations that must be carefully considered when interpreting results. Factors such as the thermal resistance of the membranes, the thermal contact resistance between the sample and the membranes, and the thermal radiation between the membranes can affect the accuracy of the technique, especially for samples with a low thermal conductivity[30, 31]. Advancements in eliminating the effect of thermal contact resistance between samples and microdevices can improve the accuracy of the measurement[32, 33]. In general, steady state techniques require precise determination of the heat transfer and temperature drop across micro/nanoscale materials, which is challenging to implement and subject to large experimental uncertainties and laborious experimental control and conduction.

In contrast, transient techniques offer the advantages of fast implementation and far less strict experimental control. Instead of analyzing the temperature response at steady state, transient techniques analyze the response in the time and frequency domains. The main thermal property extracted from transient techniques is thermal diffusivity. Due to the higher signal-to-noise ratio in the transient temperature response, the accuracy of the measured results is guaranteed, even with far less strict experimental control. One commonly used transient technique is the 3ω technique[34], which belongs to the electrothermal measurement category. It feeds a sine wave current with a frequency of ω into the sample, and the generated Joule heat and resistance change in the sample respond in 2ω, while the monitored voltage is in 3ω. By using lock-in technology to pick up the 3ω voltage, the thermal conductivity and sometimes specific heat can be accurately determined based on the voltage-frequency relation[35]. Although the thermophysical properties of coatings/films in the thickness direction are also related to energy transport at the micro/nanoscale, they are not the focus of this work. The 3ω, time-domain thermal reflectance (TDTR), laser flash, and photothermal techniques work well to measure the thermal conductivity/diffusivity in the thickness direction of coatings/films[36–45]. The transient hot wire method is commonly used to measure the thermal conductivity of liquids and powders[46, 47]. Efforts have also been made to use it to measure coatings[48].

Instead of a general review, we intend to provide very in-depth reviews of the progress in method development for 1D micro/nanomaterial characterization in Wang's lab at Iowa State University. This review covers transient electrothermal (TET) and transient photoelectro-thermal (TPET) techniques in Section 2, including their experimental principles, physical models, experimental setups, and typical applications. While these two methods are very effective in measuring most 1D

materials at the millimeter and micrometer scales, their limitations become apparent when samples are reduced to nanometer-scale thickness of μm length. Section 3 introduces the pulsed laser-assisted thermal relaxation (PLTR) technique, which overcomes the limitations of the previous two methods. Additionally, the mathematical and physical relationships among the three techniques are explained. Section 4 discusses the challenges in measuring 1D nanomaterials at the atomic level and introduces a differential concept for addressing these issues. Finally, Section 5 presents photon excitation and probing methods based on advanced Raman techniques that can measure materials of ~nm thickness and a few μm length.

2 Thermal characterization under step thermal excitation

In this section, the TET and TPET techniques are discussed in detail. Both involve step heating and electrothermal sensing. The TET technique was invented by our lab in 2007[49]. It has been shown to be very effective in measuring the in-plane thermal diffusivity of fiber- or film-like materials with high accuracy[50–53]. A schematic of the TET technique is shown in Fig. 1a. The to-be-measured sample is suspended over a trench and is secured using silver paste, which gives a good electrical and thermal connection between the sample and the electrodes. In the measurement, a transient voltage rise is induced on the sample by Joule heating using a step DC current. The transient temperature variation or, equivalently, the voltage rise (or drop) over the sample (Fig. 1c) is then used to determine the thermal diffusivity. Due to the sample's high length-to-thickness ratio, it is reasonable to assume that the heat conduction is one-dimensional along the sample. The 1D transient heat conduction along the sample (i.e., x) is governed by the following equation[49]:

$$\frac{\partial(T\rho c_{\mathrm{p}})}{\partial t} = \frac{\partial}{\partial x}\left(k\frac{\partial T}{\partial x}\right) + \dot{q},\qquad(1)$$

where ρ, c_{p}, and k are the sample's density, specific heat, and thermal conductivity, respectively. T is temperature, and $\dot{q}$ in W·m^{-3} refers to the heating induced by the electrical current. Moreover, the left end of the sample is taken as the starting point of the x-axis. The temperature distribution of the sample is then solved as[49]:

$$T(x,t) = T_0 + \frac{\alpha}{k}\int_{\tau=0}^{t}\int_{x'=0}^{L} q_0 G_{X11}\mathrm{d}x'\mathrm{d}\tau,\qquad(2)$$

where α is the thermal diffusivity and the sample length is L. G_{X11} is the Green function for pulsed heating in the sample at time τ and location x'[49],

$$G_{X11}(x,t|x',\tau) =$$
$$\frac{2}{L}\sum_{m=1}^{\infty}\exp[m^2\pi^2\alpha(t-\tau)/L^2]\sin(m\pi\frac{x}{L})\cdot\sin(m\pi\frac{x'}{L}).\qquad(3)$$

Eq. (2), as the transient temperature response over the sample, can ultimately be simplified to a normalized average temperature rise as[49]:
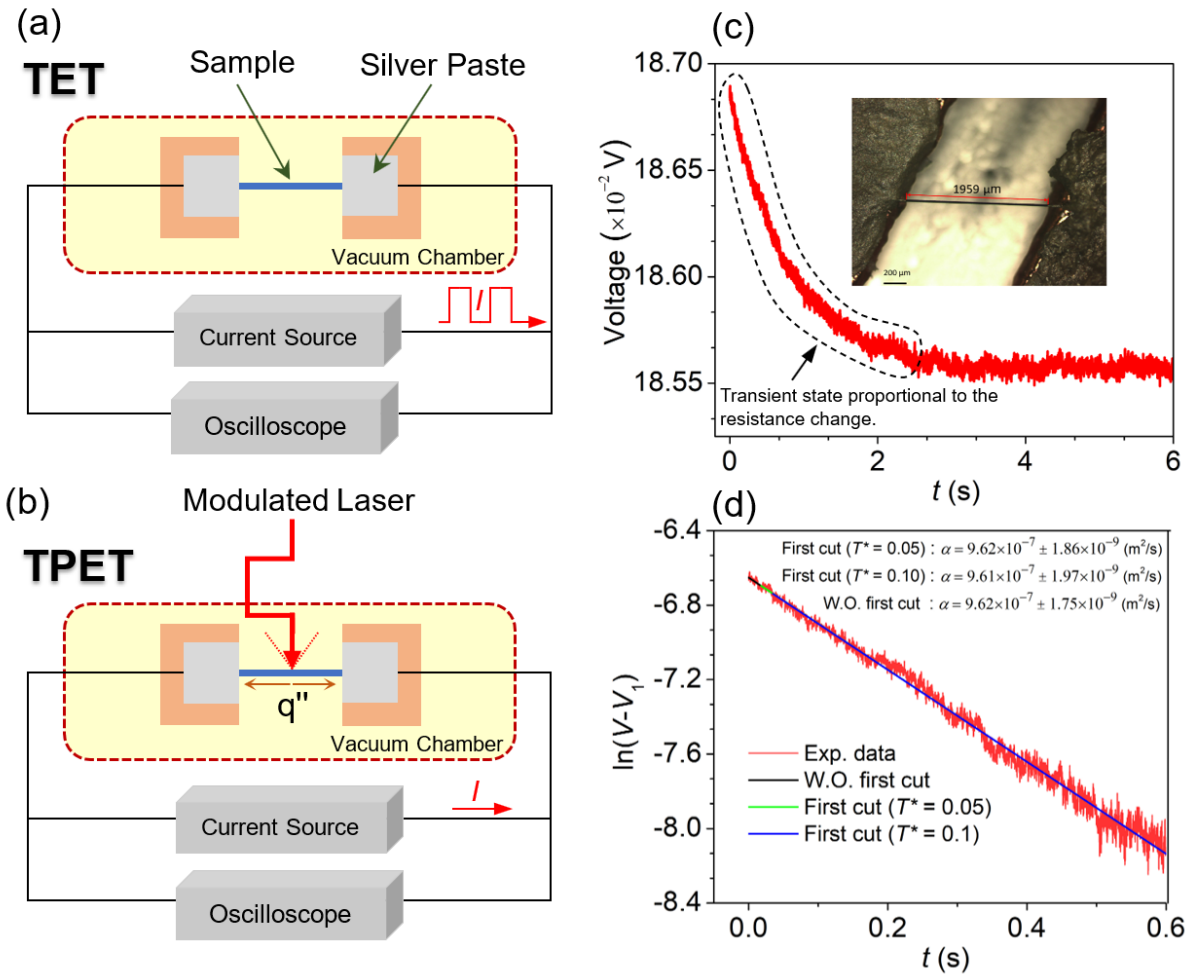
Fig. 1. (a, b) Schematic of the TET technique and TPET technique. (c) Graphene fiber TET signal with time as an example. Reproduced with permission from Ref. [54]. Copyright 2022. Elsevier. The inset is the suspended sample of 1.959 mm length. (d) Representation of the TET signal fitting: taking the natural of voltage subtracted by the steady state voltage. Reproduced with permission from Ref. [54]. Copyright 2022. Elsevier. The difference among the fittings using three different initial data treatments.

$$T^* = \frac{96}{\pi^4} \sum_{m=1}^{\infty} \frac{1 - \exp[-(2m-1)^2 \pi^2 \alpha t/L^2]}{(2m-1)^4}, \qquad (4)$$

where T^* is the normalized temperature rise with respect to the steady state temperature rise caused by the same Joule heating for the sample. It should be noted that the temperature rise is averaged over the sample's length. From the experimental data, the normalized temperature rise can be calculated as[54]:

$$T_e^* = (V_0 - V)/(V_0 - V_1), \qquad (5)$$

where V_1 is the voltage at the final steady state and V_0 is the voltage before the step heating begins. Defining the Fourier number $Fo = \alpha t/L^2$, Eq. (4) demonstrates that the normalized temperature rise versus Fo is always in the same pattern regardless of the dimension and the material of the sample[49]. Several methods can be used to determine the α of the sample once the normalized temperature rise is determined by the experiment[49]. Linear fitting at the initial stage of the experiment is one of the fitting methods. Knowing the length of the sample, it was shown that fitting the initial $Fo < 0.001$ experimental data will give a good α value[49]. The second method is

done by identifying a characteristic time (Δt_c), which is the time when T_e^* reaches 0.8665. After determining Δt_c using the $T_e^* \sim t$ curve, α can be calculated as $\alpha = 0.2026 L^2/\Delta t_c$[49]. The third method uses nonlinear global curve fitting, which uses different trial values of α to find the best fit based on the least square method. In addition to these methods, a linear fitting method was recently developed by our group[54]. It was shown that after taking the natural log of the voltage variation over time for the TET experimental data, it perfectly resembles a line. Based on a detailed numerical calculation using Eq. (4), it is concluded that[54]:

$$\ln|V - V_1| = -\pi^2 \alpha t/L^2 + D. \qquad (6)$$

Based on Eq. (6), the slope of the linear fitting for $\ln|V - V_1| \sim t$ is $-\pi^2\alpha/L^2$, from which α can be easily obtained. This rigorous method not only gives the opportunity to take advantage of the simplicity of linear fitting but also results in uncertainty determination of the fitting, which is difficult to determine in nonlinear global data fitting. Since a similar relation can also be established for the TPET and PLTR techniques, their measurement fitting uncertainty can be determined rigorously in the same way. The final measurement

uncertainty will also need to include the uncertainty in length measurement, which is mostly small. It should be noted that the data falling in the T_e^* range of $0.1-0.8$ are used for the fitting via this method, as it brings about the best accuracy[54]. Fig. 1d presents the linear fitting of the signal given in Fig. 1c. The α of the sample (a micro-thick graphene fiber) shown in Fig. 1c is determined to be $(9.61 \times 10^{-7} \pm 1.97 \times 10^{-9})$ m$^2 \cdot$s^{-1} using the data range of $0.1 < T_e^* < 0.8$. When $T_e^* < 0.1$, some nonlinearity (even very small) arises in the data, making the fitting slightly less reliable, but the difference is still very small. As shown in Fig. 1d, if we use the data of $0.05 < T_e^* < 0.8$ and $T_e^* < 0.8$ to do the fitting, the α value is determined to be $(9.62 \times 10^{-7} \pm 1.86 \times 10^{-9})$ m$^2 \cdot$s^{-1} and $(9.62 \times 10^{-7} \pm 1.75 \times 10^{-9})$ m$^2 \cdot$s^{-1}, very close to the fitting result using the data range of $0.1 < T_e^* < 0.8$[54].

In the TET technique, heating and thermal sensing use the same step current. Sometimes this makes the experiment less controllable, especially for highly electrically conductive materials where a very high current is needed to achieve a sensible temperature/resistance/voltage change. Additionally, a high voltage has to be used for very poor electrically conductive samples, making the voltage too high to sense using an oscilloscope. The TPET technique is designed to overcome

this problem, to provide a much faster rise time of heating, and to enable the measurement of samples of very high α and short length[55]. In TPET, a step amplitude-modulated continuous wave (CW) laser is used to irradiate the whole sample (Fig. 1b). Upon laser irradiation, the temperature of the suspended sample increases, and this transient temperature rise leads to a transient change in the sample's electrical resistance as well as the voltage (Fig. 1c). To detect this transient change in temperature, a small DC current is passed through the sample. It has been proven that the optimum amount of this DC current should be equal to $0.79I_{TET}$[54] to cause the same level of transient temperature rise as TET but with the least accumulated heating. For uniform thermal excitation, the temperature (voltage) evolution is the same as that in the TET method. This voltage evolution is then used to obtain α using the processing methods mentioned earlier for the TET.

Instead of irradiating the whole sample in normal TPET, the laser beam can be resized to a narrow line-shaped beam of l width for localized heating and sensing. Integrating Eq. (2) along the length of the sample results in Eq. (4) for both the TET and the TPET with uniform heating. Now, if the laser beam with a width of l irradiates the sample at location x, the normalized temperature rise would be[54]:

$$T^* = \frac{1}{Z} \sum_{m=1}^{\infty} \left\{ \frac{\cos[(2m-1)\pi x/L] - \cos[(2m-1)\pi(x+l)/L]}{(2m-1)^4} [1 - \exp(-(2m-1)^2 \pi^2 \alpha t/L^2)] \right\}, \tag{7}$$

where

$$Z = \sum_{m=1}^{\infty} \left\{ \frac{\cos[(2m-1)\pi x/L] - \cos[(2m-1)\pi(x+l)/L]}{(2m-1)^4} \right\}. \tag{8}$$

Using this localized heating, the α distribution along the sample's length can be obtained. It was shown that if this localized laser beam irradiates the sample in a range of $x \sim (0.2L - 0.8L)$, Eq. (6) can still be used to obtain α with negligible dependence on laser heating location if the sample has no spatial variation in its thermophysical properties[54]. In fact, it has been proven that for localized laser heating, in a large portion of the data in the time domain, Eq. (6) is still applicable. One merit of this TPET scanning is that if the measured α has a certain distribution against the laser heating location, then such a distribution can be used to obtain the likely patterns for some of the properties (e.g., temperature coefficient of resistivity) the sample may have.

The TET and TPET techniques are both very potent for measuring the thermal properties of a large variety of micro/nanoscale wires and films, whether they are conductive or nonconductive. However, they have advantages over each other from different viewpoints. The TPET, for instance, can be applied to extremely large or low-resistance samples. Additionally, the thermal excitation during TPET measurement has nothing to do with the electrical contact resistance. Another advantage of the TPET is that the step laser excitation could be much faster than the step electrical current used during TET measurement. The TET, on the other hand, has controlled and well-defined and known heating for a great variety of samples, which can simply be calculated as I^2R. R

is the resistance of the sample, and I is the magnitude of the step current. Moreover, the effective thermal conductivity (k_{eff}) of the sample can be obtained using the sample's steady state temperature rise as $k_{eff} = I^2RL/(12A_c\Delta T)$[56], where A_c is the sample's cross-sectional area and ΔT is the average steady state temperature rise over the sample. This ΔT can be evaluated as $\Delta R/(dR/dT)$, where ΔR can be calculated from the TET voltage change. Fitting calibrated $(R-T)$ data points will obtain dR/dT. Once k_{eff} is calculated and α_{eff} is obtained by fitting the TET signal, $(\rho c_p)_{eff}$ of the sample can be determined. This is quite a unique capability since there are very few techniques that can measure the specific heat of extremely lightweight nanoscale materials. For instance, for a sample of 1 mm length, 2 μm diameter, and 2000 kg$\cdot$m^{-3} density, its mass is only 6.2×10^{-9} g. The specific heat of such a sample can be readily measured using the TET technique. Using the TET method, Zhu et al.[56] measured the thermal properties of a type of 3C-SiC nanocrystalline microfiber called LCVD-FFF of 1495 μm length and 34.29 μm diameter coated with a 20 nm Ir layer. The α_{eff} and k_{eff} of the sample were measured to be 2.89 mm$^2 \cdot$s^{-1} and 5.59 W$\cdot$m$^{-1} \cdot$K^{-1} at room temperature, from which the $(\rho c_p)_{eff}$ of the sample was determined as 1.94×10^6 J$\cdot$m$^{-3} \cdot$K^{-1}. In another study by Deng et al.[57], three samples of carbon nanocoils (CNCs) were characterized via the TET technique. The range of the line diameter and total length of the CNCs are on the order of 300–500 nm and 100 μm, respectively. The corresponding α_{eff} values of these samples were 1.58 mm$^2 \cdot$s^{-1}, 2.7 mm$^2 \cdot$s^{-1}, and 4.11 mm$^2 \cdot$s^{-1}, and the k_{eff} values were 1.67 W$\cdot$m$^{-1} \cdot$K^{-1}, 2.77 W$\cdot$m$^{-1} \cdot$K^{-1}, and 3.20 W$\cdot$m$^{-1} \cdot$K^{-1} at 290 K. Having the α_{eff} and k_{eff} values of the samples and assuming ρ to be 2200 kg$\cdot$m^{-3}, the

average c_p of the CNC was reported to be 910 J·kg⁻¹·K⁻¹ at 290 K. DNA fiber $(\rho c_p)_{eff}$ at 190 K was reported to be 7.3×10^5 J·m⁻³·K⁻¹ calculated using $\alpha_{eff} = 0.605$ mm²·s⁻¹ (from TET) and $k_{eff} = 0.44$ W·m⁻¹·K⁻¹[58]. The length and width of the fiber were 0.405 mm and 3.47 μm, respectively. The aforementioned studies reveal how powerful the TET technique is in thermophysical property characterization of low-dimensional fiber- or film-like materials. These fibers and films are of a wide variety. This variety includes polyacrylonitrile (PAN) wires (Fig. 2a), carbon nanocoils (Fig. 2b), 3C crystalline SiC microwires (Fig. 2c), carbon nanotubes (Fig. 2d), and chemical vapor decomposition (CVD)-grown graphene supported on poly(methyl methacrylate)

(PMMA)[59]. Table 1 presents more details about these micro/nanoscale samples.

In this section, the merits and drawbacks of the TET and TPET techniques over each other are discussed. In the next section, the PLTR technique as a potent technique to overcome some common limitations of the TET and TPET techniques will be discussed in detail. The α_{eff} values summarized in Table 1 have an uncertainty of ±10% based on the global TET fitting.

3 Nanosecond pulsed thermal excitation and relaxation

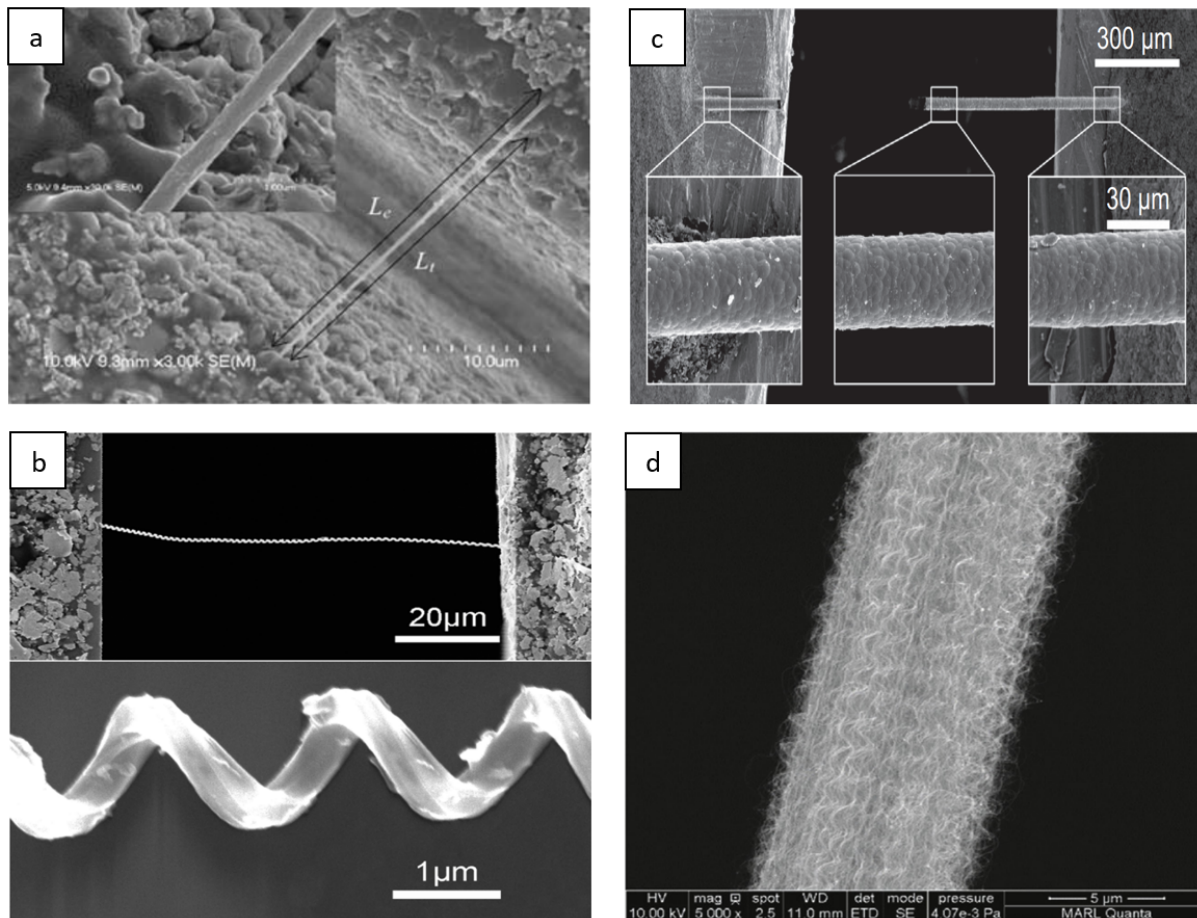While the physical principle underlying the TET/TPET

Fig. 2. (a) SEM images of single polyacrylonitrile (PAN) wires. Reproduced with permission from Ref. [60]. Copyright 2007. Springer Nature. (b) SEM images of carbon nanocoils (CNCs). Reprinted with permission from Ref. [57]. Copyright 2016. American Chemical Society. (c) SEM images of 3C crystalline silicon carbide (SiC) microwires. Reproduced with permission from Ref. [56]. Copyright 2018. Elsevier. (d) SEM images of carbon nanotube (CNT) bundles. Reproduced with permission from Ref. [61]. Copyright 2018. Elsevier.

Table 1. Details of the micro/nanoscale sample characterized via TET.

Sample	Diameter/Thickness (μm)	Length (μm)	α_{eff} (mm²·s⁻¹)@~ 290 K
PAN wires[60]	~ 0.32 − 4.62	~ 23 − 126	0.135 − 0.177
CNCs[57]	0.334	142	1.58
SiC microwires[56]	34.29	1495	2.89
CNT bundles[61]	222 − 280	2370 − 2770	13.2 − 29.6
CVD graphene on PMMA[59]	0.45–1.74 nm thick graphene on 630–826 nm thick PMMA	~ 2000	0.5 − 1.3

techniques is applicable to a wide range of 1D micro/nano-scale materials, practical implementation requires electronic devices to supply a current and/or measure the sensing voltage. Unfortunately, the slow rise time (on the order of microseconds) of the current source and amplitude-modulated laser sources can severely limit the measurement capabilities of the TET/TPET techniques, as they rely on detecting the Joule/photon heating-induced voltage change. In particular, when the sample has a short thermal characteristic time (L^2/α) falling within the same time span as the rise time, it can be difficult to differentiate the heating effect from the device's rise time. Moreover, continuous heating of the sample in the TET/TPET techniques can cause extensive heat generation and conduction to the electrodes, leading to a continuous temperature rise and potential damage to the sample if the electrode support has poor heat dissipation capability or the sample has a high thermal conductivity that needs high electrical heating to induce a sensible resistance change. Currently, current and amplitude-modulated laser sources with faster rise times are becoming more available and can be used to overcome the above challenges. Here, the PLTR technique[62–66] overcomes these limitations by using an ultrafast heat source at the nanosecond or even picosecond timescale and focusing on detecting the relatively longer cooling process.

The ultrashort duration of the heating period introduces minimal heat into the sample, significantly reducing the risk of sample damage. Additionally, this technique has no continuous heating effect and is applicable to a wide range of materials.

Fig. 3a and b shows the experimental principle of the PLTR technique. Similar to those in the TPET technique, a 1D sample is suspended between two electrodes, and a small constant DC is passed through the sample to monitor changes in voltage/resistance that indicate the temperature rise. As mentioned above, in contrast to heating and voltage measurement simultaneously over a relatively long period of time, PLTR employs a nanosecond pulsed laser to introduce very short-time heating into the sample and records the subsequent cooling process. The small DC current provides a steady and constant temperature rise in the sample without affecting the temperature rise evolution θ_{PLTR} caused by pulsed laser heating $\dot{q}_{\text{pulse}}$. Moreover, the cooling process in the length direction of the 1D sample is typically much slower than the nanosecond-scale heating duration. Consequently, the governing equation for 1D heat conduction is given by:

$$\frac{\partial (\rho c_p \theta_{\text{PLTR}})}{\partial t} = k \frac{\partial^2 \theta_{\text{PLTR}}}{\partial x^2} + \dot{q}_{\text{pulse}}, \tag{9}$$
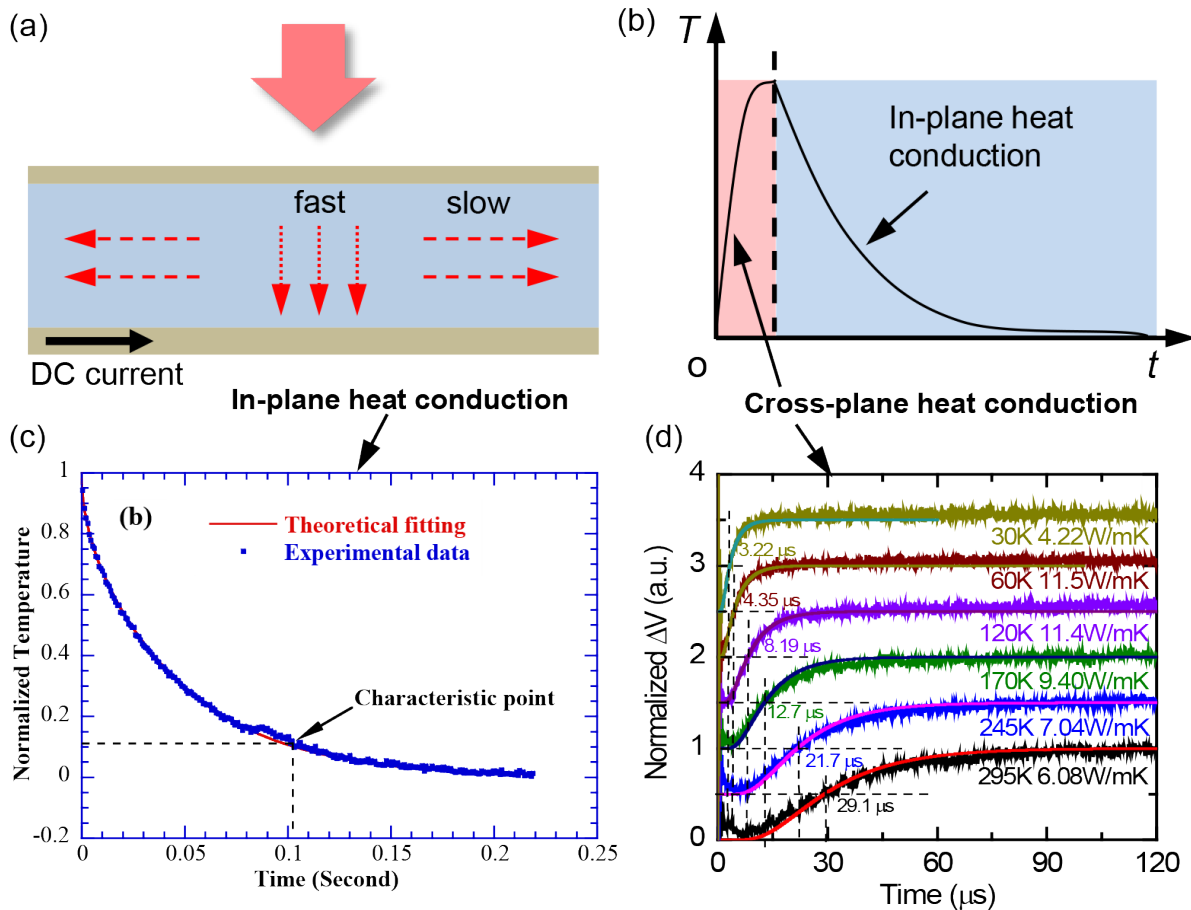

Fig. 3. (a–c) The PLTR technique in the physical principle, schematics of the temperature response at the back side of the sample, and typical experimental data and fitting curve for in-plane heat conduction, respectively. Reproduced with permission from Ref. [65]. Copyright 2008. World Scientific Publishing. (d) Typical experimental data and fitting for cross-plane heat conduction. Reproduced with permission from Ref. [63]. Copyright 2017. Elsevier.

$$\dot{q}_{\text{pulse}} = \begin{cases} \dot{q}_0, & 0 \leqslant t \leqslant \Delta t; \\ 0, & t \geqslant \Delta t; \end{cases} \quad (10)$$

where $\dot{q}_{\text{pulse}}$ is composed of two parts: during the pulse duration Δt, the heating intensity is assumed to be a constant of $\dot{q}$; zero heating occurs after the laser pulse. With boundary conditions $\theta_{\text{pulse}}(x = 0, t) = \theta_{\text{pulse}}(x = L, t) = 0$ and the initial condition $\theta_{\text{pulse}}(x, t = 0) = 0$, the solution to Eq. (9) for $t \geq \Delta t$ is

$$\theta_{\text{PLTR}}(t) = \frac{8\dot{q}_0 L^2}{k\pi^4} \sum_{m=1}^{\infty} \frac{e^{-(2m-1)^2\pi^2\alpha t/L^2}}{(2m-1)^4} \times \left(e^{-(2m-1)^2\pi^2\alpha\Delta t/L^2} - 1\right), \quad t \geqslant \Delta t. \quad (11)$$

By normalizing θ_{PLTR} with respect to the maximum temperature rise $\theta_{\text{PLTR,max}}$ immediately after pulse heating, the resulting normalized temperature evolution θ^*_{PLTR} is given as:

$$\theta^*_{\text{PLTR}}(t) = \frac{8}{\pi^2} \sum_{m=1}^{\infty} \frac{e^{-(2m-1)^2\pi^2\alpha t/L^2}}{(2m-1)^2}. \quad (12)$$

Fig. 3c shows a typical normalized temperature rise in the PLTR measurement. The thermal diffusivity can be determined by global data fitting based on Eq. (12) or characteristic point evaluation as $\alpha = 0.2026L^2/t_c$, where t_c is the time taken for θ^*_{PLTR} to decrease to 0.1097[65, 66].

Technically, heat conduction after laser pulse heating occurs simultaneously in both the thickness and length directions of the sample, as shown in Fig. 3a. However, due to the high aspect ratio of the 1D sample, a thermal steady state is very quickly established in the thickness direction, which typically requires several orders of magnitude less time than cooling in the axial direction. In other words, the temperature at the back side of the sample will increase first according to the cross-plane heat conduction from the heated front surface and then decreases due to in-plane cooling to heat sinks (Fig. 3b). As a result, it is possible to distinguish cooling in the thickness and length directions, as depicted in Fig. 3a. Similar to the flash technique, the cross-plane thermal diffusivity can be determined as:

$$\alpha_{\text{cross-plane}} = 1.38D^2/(\pi^2 t_{1/2}), \quad (13)$$

where D is the thickness of the sample and $t_{1/2}$ is called the "half-rise time", which is the time for the back side of the sample to reach half of the maximum temperature rise. Fig. 3d shows the cross-plane thermal diffusivity measurement and the resulting thermal conductivity data for a 21.4 μm-thick graphene paper from 30 K to 295 K. For multilayered structures, a more complicated 1D physical model is needed to determine the thermal diffusivity. Usually, numerical heat conduction simulation is a good choice for such data processing[63].

The TET/TPET and PLTR techniques employ different functioned heat sources to introduce temperature changes in 1D materials, which are measured based on a constant resistance temperature coefficient (RTC) of metallic sensors. The thermal diffusivity of the sample is then determined using the corresponding physical model. Despite their differences, these methods are closely related from a deeper physical and mathematical standpoint, as shown in Fig. 4. Specifically, they
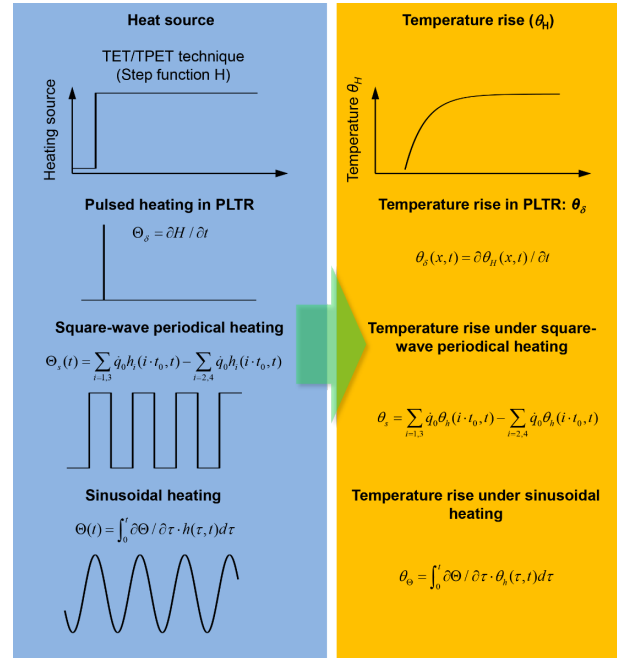

Fig. 4. Mathematical relation behind the physical models of different types of heat sources.

share the same governing equation (Eq. (9)) except for the heat source: a step function for TET/TPET and a delta function (i.e., a pulse) for PLTR.

For 1D suspended micro/nanoscale materials under heating and thermal sensing, if the step heat source is designated as $H(t) = 0$ for $t < \tau$ and $H(t) = \dot{q}_{H,0}$ for $t \geqslant \tau$, the temperature rise solution of $\theta_H(x,t)$ takes the form of the TET and TPET techniques (Eq. (4)). For the PLTR technique, the heat source (Θ) is a delta function (δ), which can be expressed as $\Theta_\delta = \partial H/\partial t$. Since the heat conduction equation is a linear equation, the resulting temperature rise solution $\theta_\delta(x,t)$ can be expressed as $\theta_\delta(x,t) = \partial\theta_H(x,t)/\partial t$.

For measuring the thermal conductivity/diffusivity of 1D micro/nanoscale materials under any arbitrarily defined heat source $\Theta(t)$, such as the 2ω heat source in the 3ω technique[35, 67], the heat source can be expressed as a summation of unit step functions $h(\tau, t)$ as $\Theta(t) = \int_0^t \partial\Theta/\partial\tau \cdot h(\tau, t)\mathrm{d}\tau$. Consequently, the temperature rise can be expressed as $\theta_\Theta = \int_0^t \partial\Theta/\partial\tau \cdot \theta_h(\tau, t)\mathrm{d}\tau$, with θ_h being the temperature rise under $h(t)$. This mathematical treatment can be applied to other amplitude-modulated heat sources, such as square wave heating used in photothermal methods[43, 68, 69], frequency-resolved Raman (FR-Raman)[70], and frequency domain energy transport-state resolved Raman (FET-Raman)[71, 72]. For a square wave heat source, since there is a step change of the heat source as $\Theta_s = \dot{q}_0$ for $0 < t < t_0$ and $\Theta_s = 0$ for $t_0 \leqslant t \leqslant 2t_0$ within a period $2t_0$, this heat source can be expressed as $\Theta_s(t) = \sum_{i=1,3} \dot{q}_0 h_i(i \cdot t_0, t) - \sum_{i=2,4} \dot{q}_0 h_i(i \cdot t_0, t)$, where $h_i(\tau)$ is a unit step function whose step change occurs at $\tau = i \cdot t_0$. Therefore, the resulting temperature rise can be expressed as $\theta_s = \sum_{i=1,3} \dot{q}_0 \theta_h(i \cdot t_0, t) - \sum_{i=2,4} \dot{q}_0 \theta_h(i \cdot t_0, t)$. This mathematical

conversion makes it straightforward to construct the solution of heat conduction under an arbitrary heat source based on a simple temperature rise solution under step heating. Additionally, since the temperature rise under step heating can be tabulated for discrete moments (Δt, $2\Delta t$, $3\Delta t$,...) in the time domain, the temperature rise under an arbitrary heat source can be obtained by simple mathematical summation, leading to superior computational efficiency.

4 Differential concept for down to atomic-level characterization

In the TET or TPET measurements, the samples need to be suspended between two electrodes. Due to their relatively weak structure, nanometer-thick materials cannot be directly suspended. To overcome this problem, the differential TET technique[58, 73, 74] has been developed to measure the in-plane thermal conductivity of nanostructures. In the experiment, a

low-dimensional material with a low thermal conductivity is used as the substrate to support the to-be-measured ultrathin film, as shown in Fig. 5a. The effective thermal diffusivity (α_{eff}) of this composite structure can be characterized by using the TET technique. First, the substrate is deposited with one layer of film with a thickness δ_c, and the effective thermal diffusivity of the thin structure-substrate system is measured as $\alpha_{eff,1}$. Then the same procedure is repeated (depositing another layer of δ_c thickness and measuring α_{eff}) n times. Fig. 5b shows the results for the α_{eff} of a glass fiber-Ir coating structure. From Fig. 5b, it is clear that α_{eff} changes linearly against R^{-1}. Finally, it is possible to establish the relationship between $\alpha_{eff,n}$ and the number of layers. The thermal conductivity of the thin structure can be determined by establishing heat conduction models for the thin structure-substrate system. If the thin structure cannot be easily coated multiple times, we will be only able to measure $\alpha_{eff,1}$ and then subtract the influence of the substrate. More details can be found in
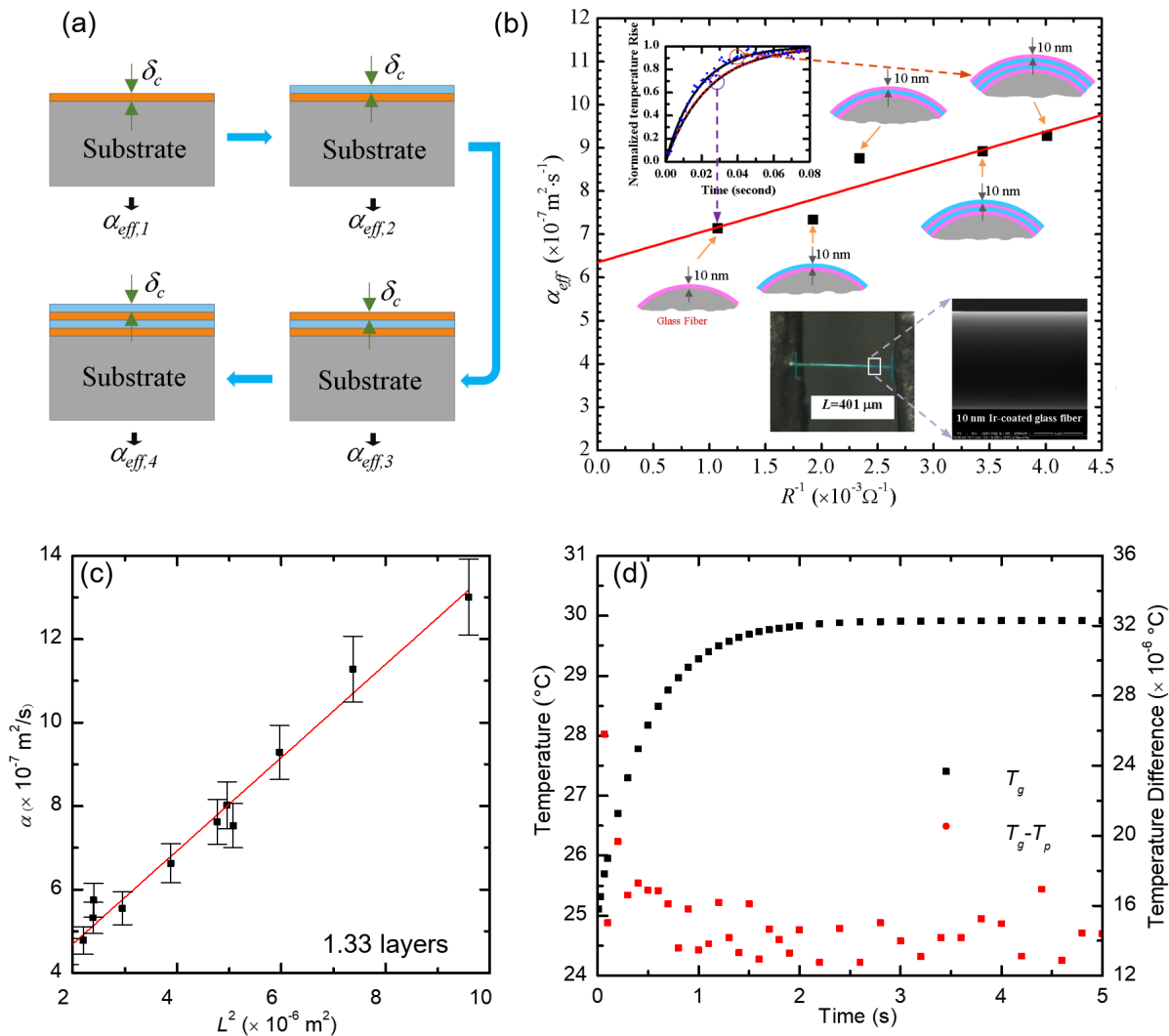

Fig. 5. (a) The cross-sectional schematic of a substrate with different nanofilm layers deposited. (b) Variation of the effective thermal diffusivity of an Ir-coated glass fiber against the inverse of the electrical resistance for 6.4 nm Ir layers coated on the glass fiber. (c) Linear fitting of $\alpha_{eff} \sim L^2$ for 1.33-layered graphene on PMMA. (d) Graphene temperature evolution with time and the temperature difference between PMMA and graphene in the middle point of the length direction. (b) Reprinted with permission from Ref. [75]. Copyright 2013. John Wiley and Sons Small. (c, d) Reproduced with permission from Ref. [59]. Copyright 2016. The Royal Society of Chemistry.

Refs. [59, 75].

When a step current is applied to the thin structure-substrate system, heat is transferred from the thin structure to the substrate, but the temperature difference between them is negligible compared with the temperature rise of the sample and has a negligible effect on the TET measurement. Fig. 5d shows the numerical simulation results of the graphene temperature variation with time and the temperature difference between PMMA and graphene in the middle of the axial direction. This is for a 1.54 mm long PMMA film of 790 nm thickness on which monolayer graphene is deposited. It can be seen that the overall temperature of the graphene increased by ∼ 5 °C. The temperature difference between PMMA and graphene is approximately 10^{-5} °C. Therefore, the temperature of graphene and PMMA could be treated the same during Joule heating. In the case of a PMMA substrate ($k = 0.2$ W·m^{-1}·K^{-1}) with a width of 1 mm, length of 2 mm, and thickness of 0.5 μm, we can estimate that its thermal resistance along the length direction is 2×10^7 K·W^{-1}, and the total thermal resistance between the graphene layer and substrate is 0.5 K·W^{-1} for a thermal contact resistance of $R_{tc}'' = 10^{-6}$ K·m^2·W^{-1}. Therefore, the thermal resistance along the length direction is much larger than that along the thickness direction. The temperature rise of the sample is mainly affected by the length direction heat conduction. In the thin structure-substrate system, when heat is transferred from the film to the substrate, the characteristic time to reach thermal equilibrium is $\Delta t_1 = \delta_c (\rho c_p)_{eff} R_{tc}''$, where δ_c is the film's thickness. The characteristic thermal diffusion time in the length direction is $\Delta t_2 \approx L^2/\alpha$. In the case of a $\delta_c = 10$ nm thick film on a PMMA substrate with a length of 1 mm and a thickness of 0.5 μm, $R_{tc}'' = 10^{-6}$ K·m^2·W^{-1}, $(\rho c_p)_{eff}$ of 2×10^6 J·m^{-3}·K^{-1}, and Δt_1 is 20 ns. The order of α is approximately 10^{-6}–10^{-3} m^2·s^{-1}, so Δt_2 is estimated to be 1 ms to 1 s. It is obvious that Δt_2 is much longer than Δt_1. Consequently, in the TET measurement, the time for the cross-sectional heat conduction to reach thermal equilibrium can be negligible.

α_{eff} is an effective value that combines the effects of the substrate, the coating, and thermal radiation. Thus, it can be written as[49, 58, 75, 76]:

$$\alpha_{eff} = \frac{\delta_c k_c + \delta_s k_s}{\delta_c (\rho c)_c + \delta_s (\rho c)_s} + \frac{1}{(\rho c_p)_{eff}} \frac{M \varepsilon \sigma T_0^3}{\delta_s + \delta_c} \frac{L^2}{\pi^2}, \quad (14)$$

where ε, σ, and δ are the emissivity, Stefan-Boltzmann constant, and thickness, respectively. Subscripts "s" and "c" represent substrate and coating, respectively. L and T_0 are the sample length and initial temperature, respectively. $M = 16$ for circular cross-section substrates and $M = 8$ for substrates with rectangular cross-sections. Here, $(\rho c_p)_{eff} = [\delta_c (\rho c)_c + \delta_s (\rho c)_s]/(\delta_c + \delta_s)$.

To eliminate the influence of radiation, TET experiments need to be conducted using the same sample of different lengths. According to Eq. (14), we can see that α_{eff} and length square (L^2) have a linear relationship. The intercept at the y-axis of the $\alpha_{eff} \sim L^2$ relationship is the real thermal diffusivity of the sample. To demonstrate this physics, the $\alpha_{eff} \sim L^2$ linear fitting for the graphene sample supported by PMMA (1.33 layers on average) of different lengths is shown in Fig. 5c.

With the knowledge of the fitting slope, PMMA substrate thickness, and temperature, the emissivity of the graphene samples can also be determined by dividing the slope by $8\sigma T_0^3 / \left[(\rho c_p)_{eff} \cdot (\delta_s + \delta_c) \pi^2 \right]$.

For the glass fiber measured in Ref. [75], where the thermal conductivity of ultrathin Ir coating is determined, the impact of thermal radiation is negligible due to its short length. If the length of the glass fiber is long, the impact of thermal radiation cannot be neglected. It should be noted that if the substrate is very thin or has a low thermal conductivity, the thermal radiation effect will become much weaker when the Ir coating thickness increases. The emissivity of glass fiber is approximately 1 and much less than 0.1 for Ir. When layers of coating are added, the emissivity of the thin structure-substrate system will be reduced, resulting in a decrease in the thermal radiation effect. Therefore, as the film thickness increases, there may be a decrease in α_{eff}, which could overshadow the effect of the coating. This problem can be solved by measuring samples of the same coating thickness but different lengths so as to subtract the influence of thermal radiation.

It is clear in Eq. (14) that if the substrate has a low thermal conductivity and thin thickness, the increase in α_{eff} will be more preeminent when the film thickness is increased. Therefore, in the differential TET technique, substrates of low thermal conductivity and thin thickness are preferred to maximize the measurement sensitivity.

5 Photon excitation and probing: Raman scattering

As mentioned earlier, in the TET, TPET, and PLTR techniques, the transient temperature rise of the sample leads to a transient change in the sample's electrical resistance. Therefore, in all the abovementioned techniques, the voltage variation across the sample is used to measure the thermal properties of the sample[41, 49, 55, 65, 66, 77–79]. A linear relation is required between the changes in temperature and resistance. Since the needed temperature rise in measurement is small (a few to 10 degrees), such a linear relation usually holds true even for materials with a nonlinear temperature-resistance relation over a large temperature range (e.g., 300 K)[80]. Such electrical sensing sometimes requires very difficult sample preparation, especially for nm-thick wires/tubes/films and very low electrical resistance samples. Additionally, for samples whose resistance has a very weak or no response to temperature change, these techniques become difficult/impossible to use. The Raman-based techniques reviewed in this section are designed to resolve the above problems (even not completely).

To date, Raman scattering has been used extensively for thermal probing and measuring the thermal properties of 2D materials such as graphene, in which measuring the exact temperature rise and the sample's laser absorption during heating are required[81–84]. Various studies have used very different optical absorption values, which is a major source of uncertainty in Raman-based techniques. In addition, for 1D nanoscale materials such as nanotubes, such measurements become almost impossible since precise determination of laser beam absorption in the material cannot be conducted

with sound confidence. For example, CNT chirality, defect level, and whether they are single or in bundles strongly affect how much laser power is absorbed in the nanotube. Hsu et al.[85] measured the optical absorption of single-walled carbon nanotubes (SWCNTs). A large number of factors have to be considered and treated for evaluating the heat flux caused by laser beam absorption, and quite large uncertainties arise in the estimation.

To eliminate the need for an exact temperature rise and laser absorption evaluation in Raman-based experiments for 2D nanoscale materials, different Raman techniques have been developed in our lab, such as ET-Raman, frequency-resolved Raman (FR-Raman), and FET-Raman[52, 70, 71, 86–89].

The ET-Raman technique uses two distinct energy transport states in both space and time domains to study the thermal response of the sample: the near zero-transport case using picosecond or nanosecond (ps or ns) lasers and the steady state case using a CW laser. The FR-Raman uses an amplitude-modulated laser with a square-wave form in a wide range of frequencies for both heating and Raman probing[70, 89]. The FET-Raman was developed based on the ET-Raman and FR-Raman to measure the thermal properties of materials. It uses a CW laser and amplitude-modulated square-wave laser (FR) with a specific frequency, as shown in Fig. 6a and b[52, 71]. Since it uses exactly the same configuration for both CW and FR situations, the laser absorption is exactly the same for both cases. In addition, the FR case makes the signal very stable and strong to collect.

Herein, we present the FET-Raman technique used to measure the thermal diffusivity of suspended well-aligned 1D SWCNTs over a silicon substrate trench using a 50× objective lens at 257 K. The sample consists of SWCNT bundles with a length of 11 μm and diameters in the range of 1.61 nm to 6.70 nm, which are composed of a few individual SWCNTs. The diameter of the laser spot under a 50× objective lens is 1.4 μm, covering several SWCNT bundles. In both CW and FR laser states, the laser irradiates the sample, causes the sample's temperature to rise, and measures its Raman shift simultaneously under different laser powers (P).

Afterward, $\psi = \partial\omega/\partial P$, termed the Raman shift power coefficient (RSC), is determined for each heating state. Here, ω is the Raman wavenumber. ψ_{CW} depends on several factors, including the laser absorption coefficient (α_l), temperature coefficient of Raman shift ($\partial\omega/\partial T$), and sample thermal conductivity (k) as $\psi_{CW} \propto \alpha_l(\partial\omega/\partial T) \cdot f_1/k$. On the other hand, ψ_{FR} depends on α_l, $\partial\omega/\partial T$, k, and volumetric heat capacity (ρc_p) as $\psi_{FR} \propto \alpha_l(\partial\omega/\partial T) \cdot f_2(\alpha)/(\rho c_p)$. RSC normalization as $\Theta = \psi_{FR}/\psi_{CW}$ eliminates the effect of Raman temperature coefficients and laser absorption. Therefore, the value of Θ is only dependent on the sample's thermal diffusivity (α), which will be used to determine α.

In the CW laser state, the energy transport governing equation is[90, 91]

$$k\nabla^2 T_{CW} + \dot{q} = 0, \tag{15}$$

in which T_{CW} is the temperature rise under CW laser heating and $\dot{q}$ is the Gaussian beam heating, which is defined below[88]:

$$\dot{q}(r,z) = \dot{q}_0 \exp(-r^2/r_0^2), \tag{16}$$

in which $\dot{q}_0$ is the laser-induced heating power per unit volume in the center of the laser spot, and r_0 (μm) is the characteristic radius of the laser spot. As the laser absorption is eliminated in the Θ calculation, the real laser beam absorption effect is negligible, and the radial temperature uniformity is ensured by the sample's few-nm diameter.

In the FR laser state, the energy transport governing equation is[92]

$$k\nabla^2 T_{FR} + \dot{q} = \rho c_p(\partial T_{FR}/\partial t), \tag{17}$$

in which T_{FR} is the temperature rise in the FR laser state, and $\dot{q}$ is the same as in Eq. (16). However, at frequency f, the square-modulating duty cycle is 50%.

Solving Eqs. (15) and (17) will yield the theoretical ratio of the sample's temperature rise of the FR case to the CW case. The relationship between this theoretical ratio and the sample's thermal diffusivity can be established. By comparing theoretical and experimental ratios, the SWCNT sample's thermal
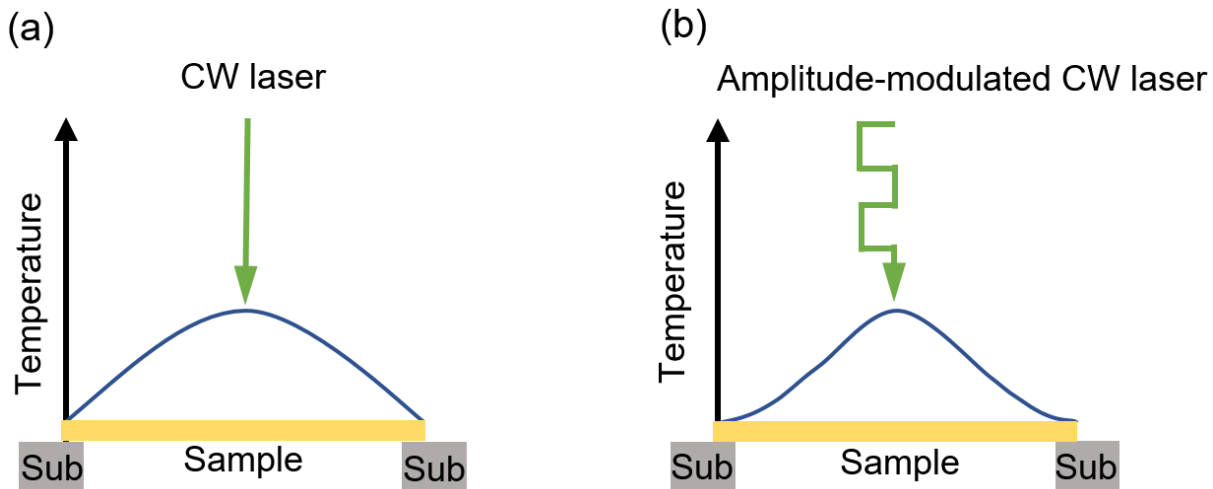

Fig. 6. Physical principle of the FET-Raman technique. (a) Temperature rise of the suspended sample under CW laser heating. (b) Amplitude-modulated laser heating.

diffusivity can be determined. Note that while simulating the 1D model, we rigorously consider the Raman intensity weighted average temperature rise over space ($\Delta \bar{T}_{CW}$) in the CW case and the Raman intensity weighted average temperature over space and time ($\Delta \bar{T}_{FR}$) in the FR case.

Since the sample might be damaged and we might not obtain a linear $\omega \sim P$ relationship at high laser powers, we keep the laser power as low as possible for both laser heating states as 1.79–17.9 mW using a 50× objective lens. To achieve the highest sensitivity of the thermal diffusivity measurement, it is important to keep Θ as close to 0.75 as possible[71]. Fig. 7a shows the 2D contour plot of the Raman shift of the G peak at ~1582 cm^{-1} at 257 K under different laser powers. For both CW and FR laser states, the Raman shift of the G peak is linearly related to the laser power at 257 K with $\psi_{CW} = (-0.161 \pm 0.007)$ cm$^{-1} \cdot$mW^{-1} and $\psi_{FR} = (-0.118 \pm 0.006)$ cm$^{-1} \cdot$mW^{-1}, which gives a Θ of 0.73 ± 0.02. It is important to note that the laser power is measured during the laser-on time, not as an average over the laser-on and off times. Fig. 7b shows the modeling result of theoretical values of Θ at 1 MHz versus thermal diffusivity α. Using this curve and the experimental Θ of 0.73, the sample's thermal diffusivity is determined to be $(6.54 \pm 0.03) \times 10^{-5}$ m$^2 \cdot$s^{-1} at 257 K.

The ET-Raman can also be used to measure 1D micro/nanoscale materials. Because a pulsed laser provides very intense photon heating in a very short time and the pulse-pulse interference is low since the temperature rise caused by one heating pulse can be quite relaxed before the next pulse comes in, the physical sensitivity of the ET-Raman is higher than that of the FET-Raman. However, it might damage the sample due to intense pulse heating. Furthermore, involving more intense laser heating during the very short time in the ET-Raman could exceed the absorption saturation level, meaning that the sample will not absorb any more laser, which is not preferred. The advantage of ET-Raman is that we can go to an extremely small time domain (ps) if a picosecond laser is used for heating[86–88]. Due to the same laser-on

and off times in FET-Raman, the sample may not completely cool down after one laser heating before the next heating interval, resulting in decreased sensitivity.

6 Concluding remarks and perspectives

The transient techniques developed in Wang's lab offer powerful means of measuring the thermophysical properties of various micro/nanoscale wires and films, with each technique having its own advantages and disadvantages. The TET technique provides controlled and well-defined heating, making it suitable for a wide range of samples. Samples with extremely high or low electrical resistance or a very fast thermal characteristic time will be very difficult to measure using the TET technique. On the other hand, the TPET technique overcomes the limitations of high electrical current/voltage that might be needed in TET and enables measurements of extremely large and low-resistance samples. However, both techniques rely on detecting the step heating-induced voltage change, which can be limited by the slow rise time of the current/laser sources. To address this limitation, the PLTR technique utilizes ultrafast heat sources (i.e., laser) at the nanosecond or picosecond timescale and probes the cooling process. The PLTR technique offers the capability of measuring very fast heat transfer processes and reduces the risk of continuous heat generation and potential damage to the sample.

TET or TPET measurements of nanometer-thick materials can be problematic because they cannot be directly suspended due to their weak structure. The differential TET technique overcomes this problem by utilizing low-dimensional materials as supportive substrates for ultrathin films, enabling the measurement of in-plane thermal conductivity in nanostructures. The TET, TPET, and PLTR techniques rely on a good electrical resistance response to temperature changes. For materials whose resistance has a weak or no response to temperature change, Raman-based techniques can be used and have been widely applied to measure 1D and 2D nanoscale materials. Wang's lab has developed Raman-based
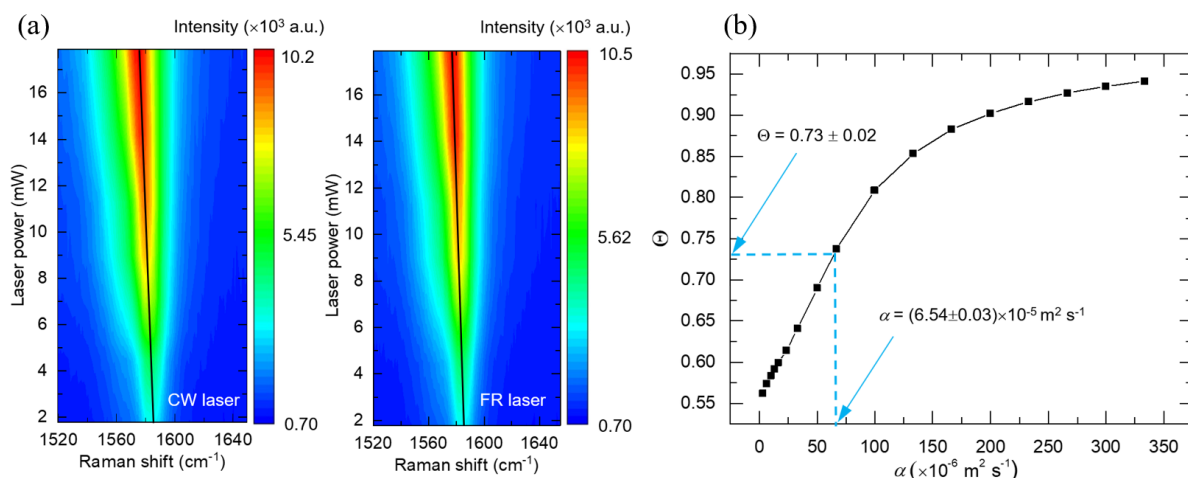

Fig. 7. (a) 2D contour plot of the Raman shift for the G peak against laser power at 257 K for SWCNT bundles. Left side: for the CW case, the slope of linear fitting, as indicated with a solid black line, is $\psi_{CW} = (-0.161 \pm 0.007)$ cm$^{-1} \cdot$mW^{-1}. Right side: for the FR case, the slope of linear fitting, as indicated with a solid black line, is $\psi_{FR} = (-0.118 \pm 0.006)$ cm$^{-1} \cdot$mW^{-1}. (b) Theoretical values of the temperature rise ratio at 1 MHz from numerical modeling against the thermal diffusivity. Using the normalized RSC (Θ) from the experiment, the thermal diffusivity of SWCNTs can be interpolated, as indicated by the blue dashed line.

techniques, such as ET-Raman, FR-Raman, and FET-Raman, eliminating the need for precise temperature rise and laser absorption evaluation. On the other hand, these Raman techniques will have low signals when the temperature is high. For samples with easy photofluorescence excitation, Raman-based techniques are difficult to use since the fluorescence signal can easily overshadow the Raman signal. For wide bandgap materials with a very strong Raman signal but negligible laser absorption, Raman-based techniques cannot be used directly since the Raman laser will not cause simultaneous heating. For such a scenario, a very thin material (e.g., few-layered graphene) can be coated on the sample for both excellent Raman excitation and laser absorption/heating purposes.

Thermophysical property measurements at the micro/nanoscale still face significant challenges caused by extremely high or low thermal conductivity, material geometry, and material size. Additionally, studying the variation of thermophysical properties against temperature from very low (a few K) to very high levels (1000 K or higher) requires additional and rigorous technical and scientific considerations and design. Such a temperature effect is of great engineering and science interest in device and material design and optimization. Generally speaking, transient techniques offer great advantages over steady state techniques for several reasons. Steady state techniques usually require precise control and determination of the heat flux and temperature difference across the sample. Such experimental control is often very challenging and subject to large uncertainties. Transient techniques, however, have no such limitation. Most times, it only needs size information about the sample and its relative temperature response, which can be readily obtained. We foresee that transient Raman techniques, including the ET-Raman and FET-Raman, will see broad adoption and provide unprecedented measurement capability and physics knowledge about 1D micro/nanoscale materials.

Acknowledgements

Conflict of interest

The authors declare that they have no conflict of interest.

Biographies

Amin Karamati   is pursuing his Ph.D. degree in Mechanical Engineering at Iowa State University since 2021. He received his M.S. and B.S. in Mechanical Engineering from K. N. Toosi University of Technology, Iran, in 2016 and 2013, respectively. Thermal transport in 1D scale has been his research focus. Currently, he is conducting research on the thermal characterization of micro/nanowires using Raman Spectroscopy, TET, and TPET techniques.

Shen Xu   is a Professor of Shanghai University of Engineering Science.
She received her B.S. from East China University of Science and Technology in 2008, M.S. from Fudan University in 2011, and her Ph.D. degree from Iowa State University in 2015. Her research interests cover energy transfer at the micro/nanoscale, heat transfer behavior of new materials and complex nanostructures, and multiphysics in the coupling of optical and temperature fields. She has developed the first time-domain differential Raman (TD-Raman) and frequency-resolved Raman (FR-Raman) techniques for high accuracy measurement of thermal conductivity and diffusivity of atomic-scale materials.

Huan Lin   is a Professor in Engineering Thermophysics at Qingdao University of Technology. She obtained her Ph.D. degree from the College of Engineering, Ocean University of China in 2014, M.S. (2008) from Beijing Institute of Technology and B.S. (2006) from Shandong University of Technology. Her current research focuses on thermal characterization of micro and nano materials. She has developed the differential TET technique for measuring thermal conductivity of fibers and films down to ~nm scale, and conducted the first characterization of in-plane structure thermal domain size of 2D materials.

Mahya Rahbar   is pursuing her Ph.D. degree in Mechanical Engineering at Iowa State University in 2022. She received her M.S. and B.S. in Chemical Engineering from the University of Tehran, Iran, in 2018 and 2021. Experimental investigation of thermal transport in micro/nanoscale materials has been her research focus. Currently, she is conducting research on optical-acoustic phonon temperature difference of 2D materials using Raman Spectroscopy.

Xinwei Wang   is the Anson Marston Distinguished Professor and Wilkinson Professor in Interdisciplinary Engineering at Iowa State University. He obtained his Ph.D. degree from the School of Mechanical Engineering, Purdue University in 2001, M.S. (1996) and B.S. (1994) from the University of Science and Technology of China. Over the past 20 years, he has led his laboratory to develop new techniques for characterizing energy transport at the micro/nanoscale. His current research focuses on conjugated energy transport in 2D materials and interfaces.

References

[1] Yang S, Cheng Y, Xiao X, et al. Development and application of carbon fiber in batteries. *Chemical Engineering Journal,* **2020**, *384*: 123294.

[2] Gupta N, Gupta S M, Sharma S K. Carbon nanotubes: Synthesis, properties and engineering applications. *Carbon Letters,* **2019**, *29*: 419–447.

[3] Anzar N, Hasan R, Tyagi M, et al. Carbon nanotube—A review on synthesis, properties and plethora of applications in the field of biomedical science. *Sensors International,* **2020**, *1*: 100003.

[4] Tan D, Jiang C, Li Q, et al. Silver nanowire networks with preparations and applications: A review. *Journal of Materials Science: Materials in Electronics,* **2020**, *31*: 15669–15696.

[5] Zhu Y, Deng Y, Yi P, et al. Flexible transparent electrodes based on silver nanowires: Material synthesis, fabrication, performance, and applications. *Advanced Materials Technologies,* **2019**, *4*: 1900413.

[6] Quan L N, Kang J, Ning C Z, et al. Nanowires for photonics. *Chemical Reviews,* **2019**, *119*: 9153–9169.

[7] Nunes D, Pimentel A, Gonçalves A, et al. Metal oxide nanostructures for sensor applications. *Semiconductor Science and Technology,* **2019**, *34*: 043001.

[8] Park J, Hwang J C, Kim G G, et al. Flexible electronics based on one-dimensional and two-dimensional hybrid nanomaterials. *InfoMat,* **2020**, *2*: 33–56.

[9] Gong S, Cheng W. One-dimensional nanomaterials for soft electronics. *Advanced Electronic Materials,* **2017**, *3*: 1600314.

[10] Chen S, Zhuo M P, Wang X D, et al. Optical waveguides based on one-dimensional organic crystals. *PhotoniX,* **2021**, *2*: 1–24.

[11] VanOrman Z A, Conti C R III, Strouse G F, et al. Red-to-blue photon upconversion enabled by one-dimensional CdTe nanorods. *Chemistry of Materials,* **2021**, *33*: 452–458.

[12] Chen C, Fan Y, Gu J, et al. One-dimensional nanomaterials for energy storage. *Journal of Physics D: Applied Physics,* **2018**, *51*: 113002.

[13] Wei Q, Xiong F, Tan S, et al. Porous one-dimensional nanomaterials: Design, fabrication and applications in electrochemical energy storage. *Advanced Materials,* **2017**, *29*: 1602300.

[14] Hu K, Wang F, Shen Z, et al. Enhancement methods of hydrogen sensing for one-dimensional nanomaterials: A review. *International Journal of Hydrogen Energy,* **2021**, *46*: 20119–20138.

[15] Chen P C, Shen G, Chen H, et al. High-performance single-crystalline arsenic-doped indium oxide nanowires for transparent thin-film transistors and active matrix organic light-emitting diode displays. *ACS Nano,* **2009**, *3*: 3383–3390.

[16] Shan Q, Song J, Zou Y, et al. High performance metal halide perovskite light-emitting diode: From material design to device optimization. *Small,* **2017**, *13*: 1701770.

[17] Jeong K Y, Hwang M S, Kim J, et al. Recent progress in nanolaser technology. *Advanced Materials,* **2020**, *32*: 2001996.

[18] Haret L D, Tanabe T, Kuramochi E, et al. Extremely low power optical bistability in silicon demonstrated using 1D photonic crystal nanocavity. *Optics Express,* **2009**, *17*: 21108–21117.

[19] Jaramillo-Cabanzo D F, Ajayi B P, Meduri P, et al. One-dimensional nanomaterials in lithium-ion batteries. *Journal of Physics D: Applied Physics,* **2021**, *54*: 083001.

[20] Suba Lakshmi M, Wabaidur S M, Alothman Z A, et al. Novel 1D polyaniline nanorods for efficient electrochemical supercapacitors: A facile and green approach. *Synthetic Metals,* **2020**, *270*: 116591.

[21] Yang B, Myung N V, Tran T T. 1D metal oxide semiconductor materials for chemiresistive gas sensors: A review. *Advanced Electronic Materials,* **2021**, *7*: 2100271.

[22] Nascimento E P, Firmino H C T, Neves G A, et al. A review of recent developments in tin dioxide nanostructured materials for gas sensors. *Ceramics International,* **2022**, *48*: 7405–7440.

[23] Kaur N, Singh M, Moumen A, et al. 1D titanium dioxide: Achievements in chemical sensing. *Materials,* **2020**, *13*: 2974.

[24] Cai R, Du Y, Yang D, et al. Free-standing 2D nanorafts by assembly of 1D nanorods for biomolecule sensing. *Nanoscale,* **2019**, *11*: 12169–12176.

[25] Taloni A, Vodret M, Costantini G, et al. Size effects on the fracture of microscale and nanoscale materials. *Nature Reviews Materials,* **2018**, *3*: 211–224.

[26] Cahill D G, Braun P V, Chen G, et al. Nanoscale thermal transport. II. 2003–2012. *Applied Physics Reviews,* **2014**, *1*: 011305.

[27] Cahill D G, Ford W K, Goodson K E, et al. Nanoscale thermal transport. *Journal of Applied Physics,* **2003**, *93*: 793–818.

[28] Shi L, Li D, Yu C, et al. Measuring thermal and thermoelectric properties of one-dimensional nanostructures using a microfabricated device. *Journal of Heat Transfer,* **2003**, *125*: 881–888.

[29] Kim P, Shi L, Majumdar A, et al. Thermal transport measurements of individual multiwalled nanotubes. *Physical Review Letters,* **2001**, *87*: 215502.

[30] Dong L, Xi Q, Chen D, et al. Dimensional crossover of heat conduction in amorphous polyimide nanofibers. *National Science Review,* **2018**, *5*: 500–506.

[31] Wang C, Guo J, Dong L, et al. Superior thermal conductivity in suspended bilayer hexagonal boron nitride. *Scientific Reports,* **2016**, *6*: 25334.

[32] Wang Z, Xie R, Bui C T, et al. Thermal transport in suspended and supported few-layer graphene. *Nano Letters,* **2011**, *11*: 113–118.

[33] Aiyiti A, Bai X, Wu J, et al. Measuring the thermal conductivity and interfacial thermal resistance of suspended MoS_2 using electron beam self-heating technique. *Science Bulletin,* **2018**, *63*: 452–458.

[34] Cahill D G. Thermal conductivity measurement from 30 to 750 K: The 3ω method. *Review of Scientific Instruments,* **1990**, *61*: 802–808.

[35] Hou J, Wang X, Vellelacheruvu P, et al. Thermal characterization of single-wall carbon nanotube bundles using the self-heating 3ω technique. *Journal of Applied Physics,* **2006**, *100*: 124314.

[36] Sheindlin M, Halton D, Musella M, et al. Advances in the use of laser-flash techniques for thermal diffusivity measurement. *Review of Scientific Instruments,* **1998**, *69*: 1426–1436.

[37] Ohta H, Shibata H, Suzuki A, et al. Novel laser flash technique to measure thermal effusivity of highly viscous liquids at high temperature. *Review of Scientific Instruments,* **2001**, *72*: 1899–1903.

[38] Kim S K, Kim Y J. Determination of apparent thickness of graphite coating in flash method. *Thermochimica Acta,* **2008**, *468*: 6–9.

[39] Larson K B, Koyama K. Correction for finite-pulse-time effects in very thin samples using the flash method of measuring thermal diffusivity. *Journal of Applied Physics,* **1967**, *38*: 465–474.

[40] Lindemann A, Blumm J, Brunner M, Current limitations of commercial laser flash techniques for highly conducting materials and thin films. **2014**. https://www.oldcitypublishing.com/journals/hthp-home/hthp-issue-contents/hthp-volume-43-number-2-3-2014/hthp-43-2-3-p-243-252/.

[41] Liu J, Han M, Wang R, et al. Photothermal phenomenon: Extended ideas for thermophysical properties characterization. *Journal of Applied Physics,* **2022**, *131*: 065107.

[42] Chen X, He Y, Zhao Y, et al. Thermophysical properties of hydrogenated vanadium-doped magnesium porous nanostructures. *Nanotechnology,* **2010**, *21*: 055707.

[43] Xu S, Wang X. Across-plane thermal characterization of films based on amplitude-frequency profile in photothermal technique. *AIP Advances,* **2014**, *4*: 107122.

[44] Xu Z, Xu S, Tang X, et al. Energy transport in crystalline DNA composites. *AIP Advances,* **2014**, *4*: 017131.

[45] Jiang P, Qian X, Gu X, et al. Probing anisotropic thermal conductivity of transition metal dichalcogenides MX_2 (M = Mo, W and X = S, Se) using time-domain thermoreflectance. *Advanced Materials,* **2017**, *29*: 1701068.

[46] Stalhane B, Pyk S. New method for determining the coefficients of thermal conductivity. *Tek. Tidskr,* **1931**, *61*: 389–393.

[47] Salim S R. Thermal conductivity measurements using the transient hot-wire method: A review. *Measurement Science and Technology,* **2022**, *33*: 125022.

[48] Okuda M, Ohkubo S. A novel method for measuring the thermal conductivity of submicrometre thick dielectric films. *Thin Solid Films,* **1992**, *213*: 176–181.

[49] Guo J, Wang X, Wang T. Thermal characterization of microscale conductive and nonconductive wires using transient electrothermal technique. *Journal of Applied Physics,* **2007**, *101*: 063537.

[50] Hunter N, Karamati A, Xie Y, et al. Laser photoreduction of graphene aerogel microfibers: Dynamic electrical and thermal behaviors. *ChemPhysChem,* **2022**, *23*: e202200417.

[51] Xu S, Zobeiri H, Hunter N, et al. Photocurrent in carbon nanotube bundle: Graded Seebeck coefficient phenomenon. *Nano Energy,* **2021**, *86*: 106054.

[52] Wang R, Zobeiri H, Lin H, et al. Anisotropic thermal conductivities and structure in lignin-based microscale carbon fibers. *Carbon,* **2019**, *147*: 58–69.

[53] Xie Y, Yuan P, Wang T, et al. Switch on the high thermal conductivity of graphene paper. *Nanoscale,* **2016**, *8*: 17581–17597.

[54] Karamati A, Hunter N, Lin H, et al. Strong linearity and effect of laser heating location in transient photo/electrothermal characterization of micro/nanoscale wires. *International Journal of Heat and Mass Transfer,* **2022**, *198*: 123393.

[55] Wang T, Wang X, Guo J, et al. Characterization of thermal diffusivity of micro/nanoscale wires by transient photo-

electro-thermal technique. *Applied Physics A,* **2007**, *87*: 599–605.

[56] Zhu B, Wang R, Harrison S, et al. Thermal conductivity of SiC microwires: Effect of temperature and structural domain size uncovered by 0 K limit phonon scattering. *Ceramics International,* **2018**, *44*: 11218–11224.

[57] Deng C, Sun Y, Pan L, et al. Thermal diffusivity of a single carbon nanocoil: Uncovering the correlation with temperature and domain size. *ACS Nano,* **2016**, *10*: 9710–9719.

[58] Xu Z, Wang X, Xie H. Promoted electron transport and sustained phonon transport by DNA down to 10 K. *Polymer,* **2014**, *55*: 6373–6380.

[59] Liu J, Wang T, Xu S, et al. Thermal conductivity of giant mono- to few-layered CVD graphene supported on an organic substrate. *Nanoscale,* **2016**, *8*: 10298–10309.

[60] Guo J, Wang X, Zhang L, et al. Transient thermal characterization of micro/submicroscale polyacrylonitrile wires. *Applied Physics A,* **2007**, *89*: 153–156.

[61] Xie Y, Wang T, Zhu B, et al. 19-Fold thermal conductivity increase of carbon nanotube bundles toward high-end thermal design applications. *Carbon,* **2018**, *139*: 445–458.

[62] Feng X, Liu G, Xu S, et al. 3-dimensional anisotropic thermal transport in microscale poly(3-hexylthiophene) thin films. *Polymer,* **2013**, *54*: 1887–1895.

[63] Han M, Liu J, Xie Y, et al. Sub-μm *c*-axis structural domain size of graphene paper uncovered by low-momentum phonon scattering. *Carbon,* **2018**, *126*: 532–543.

[64] Han M, Xie Y, Liu J, et al. Significantly reducedc-axis thermal diffusivity of graphene-based papers. *Nanotechnology,* **2018**, *29*: 265702.

[65] Guo J, Wang X, Geohegan D B, et al. Thermal characterization of multi-wall carbon nanotube bundles based on pulsed laser-assisted thermal relaxation. *Functional Materials Letters,* **2008**, *1*: 71–76.

[66] Guo J, Wang X, Geohegan D B, et al. Development of pulsed laser-assisted thermal relaxation technique for thermal characterization of microscale wires. *Journal of Applied Physics,* **2008**, *103*: 113505.

[67] Lu L, Yi W, Zhang D L. 3ω method for specific heat and thermal conductivity measurements. *Review of Scientific Instruments,* **2001**, *72*: 2996–3003.

[68] Wang T, Wang X, Zhang Y, et al. Effect of zirconium(IV) propoxide concentration on the thermophysical properties of hybrid organic-inorganic films. *Journal of Applied Physics,* **2008**, *104*: 013528.

[69] Wang X, Hu H, Xu X. Photo-acoustic measurement of thermal conductivity of thin films and bulk materials. *Journal of Heat Transfer,* **2001**, *123*: 138–144.

[70] Wang T, Xu S, Hurley D H, et al. Frequency-resolved Raman for transient thermal probing and thermal diffusivity measurement. *Optics Letters,* **2015**, *41*: 80.

[71] Zobeiri H, Wang R, Wang T, et al. Frequency-domain energy transport state-resolved Raman for measuring the thermal conductivity of suspended nm-thick MoSe$_2$. *International Journal of Heat and Mass Transfer,* **2019**, *133*: 1074–1085.

[72] Zobeiri H, Wang R, Zhang Q, et al. Hot carrier transfer and phonon transport in suspended nm WS$_2$ films. *Acta Materialia,* **2019**, *175*: 222–237.

[73] Lin H, Xu S, Wang X, et al. Significantly reduced thermal diffusivity of free-standing two-layer graphene in graphene foam. *Nanotechnology,* **2013**, *24*: 415706.

[74] Lin H, Xu S, Zhang Y Q, et al. Electron transport and bulk-like behavior of wiedemann–franz law for sub-7 nm-thin iridium films on silkworm silk. *ACS Applied Materials & Interfaces,* **2014**, *6*: 11341–11347.

[75] Lin H, Xu S, Wang X, et al. Thermal and electrical conduction in ultrathin metallic films: 7 nm down to sub-nanometer thickness. *Small,* **2013**, *9*: 2585–2594.

[76] Xie Y, Xu Z, Xu S, et al. The defect level and ideal thermal conductivity of graphene uncovered by residual thermal reffusivity at the 0 K limit. *Nanoscale,* **2015**, *7*: 10101–10110.

[77] Feng B, Ma W, Li Z, et al. Simultaneous measurements of the specific heat and thermal conductivity of suspended thin samples by transient electrothermal method. *Review of Scientific Instruments,* **2009**, *80*: 064901.

[78] Xing C, Munro T, Jensen C, et al. Analysis of the electrothermal technique for thermal property characterization of thin fibers. *Measurement Science and Technology,* **2013**, *24*: 105603.

[79] Guo J, Wang X, Geohegan D, et al. Thermal characterization of micro/nanoscale wires/tubes using pulsed laser-assisted thermal relaxation. *MRS Online Proceedings Library,* **2011**, *1083*: 4.

[80] Lin H, Hunter N, Zobeiri H, et al. Ultra-high thermal sensitivity of graphene microfiber. *Carbon,* **2023**, *203*: 620–629.

[81] Faugeras C, Faugeras B, Orlita M, et al. Thermal conductivity of graphene in corbino membrane geometry. *ACS Nano,* **2010**, *4*: 1889–1892.

[82] Sadeghi M M, Pettes M T, Shi L. Thermal transport in graphene. *Solid State Communications,* **2012**, *152*: 1321–1330.

[83] Cai W, Moore A L, Zhu Y, et al. Thermal transport in suspended and supported monolayer graphene grown by chemical vapor deposition. *Nano Letters,* **2010**, *10*: 1645–1651.

[84] Chen S, Moore A L, Cai W, et al. Raman measurements of thermal transport in suspended monolayer graphene of variable sizes in vacuum and gaseous environments. *ACS Nano,* **2011**, *5*: 321–328.

[85] Hsu I K, Pettes M T, Bushmaker A, et al. Optical absorption and thermal transport of individual suspended carbon nanotube bundles. *Nano Letters,* **2009**, *9*: 590–594.

[86] Yuan P, Wang R, Tan H, et al. Energy transport state resolved Raman for probing interface energy transport and hot carrier diffusion in few-layered MoS$_2$. *ACS Photonics,* **2017**, *4*: 3115–3129.

[87] Yuan P, Tan H, Wang R, et al. Very fast hot carrier diffusion in unconstrained MoS$_2$ on a glass substrate: Discovered by picosecond ET-Raman. *RSC Advances,* **2018**, *8*: 12767–12778.

[88] Wang R, Wang T, Zobeiri H, et al. Measurement of the thermal conductivities of suspended MoS$_2$ and MoSe$_2$ by nanosecond ET-Raman without temperature calibration and laser absorption evaluation. *Nanoscale,* **2018**, *10*: 23087–23102.

[89] Wang T, Han M, Wang R, et al. Characterization of anisotropic thermal conductivity of suspended nm-thick black phosphorus with frequency-resolved Raman spectroscopy. *Journal of Applied Physics,* **2018**, *123*: 145104.

[90] Lee J U, Yoon D, Kim H, et al. Thermal conductivity of suspended pristine graphene measured by Raman spectroscopy. *Physical Review B,* **2011**, *83*: 081419.

[91] Yuan P, Liu J, Wang R, et al. The hot carrier diffusion coefficient of sub-10 nm virgin MoS$_2$: Uncovered by non-contact optical probing. *Nanoscale,* **2017**, *9*: 6808–6820.

[92] Sinha S. Thermal model for nanosecond laser ablation of alumina. *Ceramics International,* **2015**, *41*: 6596–6603.